

Vertical nutrient fluxes due to turbulent mixing in mesoscale cyclonic eddies

Bachelor Thesis

B. Sc. Physics of the Earth System:

Meteorology, Oceanography, Geophysics

Christian-Albrechts-University of Kiel

GEOMAR Helmholtz Center for Ocean Research

Author: Martin Holzapfel

Matriculation Number: 1133144

First Examiner: Dr. Marcus Dengler

Second Examiner: Dr. Torge Martin

July 2021

Abstract

Mesoscale cyclonic eddies (CEs) represent an important and abundant feature in the world's oceans. It has long been observed that CEs sustain a highly productive ecosystem within their core. The vertical nutrient transport mechanisms sustaining these ecosystems are not fully resolved yet. This study analysed microstructure profiles collected within two individual CEs in the eastern tropical North Atlantic and calculated vertical turbulent nitrate fluxes into the mixed layer. Hoping to gain insights into the turbulent structure and nutrient transport mechanisms within CEs. This study found a significant increase in the dissipation rates of turbulent kinetic energy towards the center of CE_2019_18N_20W, a CE situated within the open ocean. High dissipation rates are observed throughout CE_2019_14N_25W, which was a CE observed close to the island Brava (Cape Verde). Vertical nitrate fluxes averaged for all stations with less than 60 km distance from the center of CE_2019_18N_20W resulted in a nitrate flux of $2.65 \times 10^{-2} \mu\text{mol m}^{-2} \text{s}^{-1}$. All stations between 60 and 110 km distance from the center of CE_2019_18N_20W resulted in an average nitrate flux of $8.98 \times 10^{-3} \mu\text{mol m}^{-2} \text{s}^{-1}$. Therefore, the vertical nitrate flux within CE_2019_18N_20W was almost three times higher than on the outside of the eddy. These nutrient fluxes are amongst the highest reported for an open-ocean setting. The highly elevated turbulence within CE_2019_14N_25W led to an average nitrate flux of $1.63 \times 10^{-1} \mu\text{mol m}^{-2} \text{s}^{-1}$. Comparing the nitrate fluxes to total primary production rates (TPP) measured within the eddies showed that the flux in the inner 60 km of CE_2019_18N_20W is capable to sustain 13% of the observed TPP. The high fluxes within CE_2019_14N_25W can sustain 38% of the measured TPP. This indicates that turbulent nutrient fluxes are not the main contributor to the nutrient demand of the primary production within eddies.

Zusammenfassung

Mesoskalige cyclonale Wirbel (CW) sind ein wichtiger Bestandteil des Ozeans. Vielseitige Beobachtungen haben gezeigt, dass die Deckschicht solcher Wirbel oft eine außerordentlich hohe Primärproduktion aufweist. Die physikalischen Prozesse, welche den vertikalen Nährstoff Transport sicherstellen, welcher zum Erhalt dieser hohen Primärproduktion notwendig ist, sind noch nicht vollständig beschrieben. Diese Studie analysiert Microstruktur Profile aus zwei unabhängigen CW im östlichen tropischen Nordatlantik und berechnet turbulente vertikale Nitrat Flüsse in die Deckschicht der CWs. In Richtung des Zentrums von CE_2019_18N_20W, einem CW im offenen Ozean, wurde ein signifikanter Anstieg der Dissipationsraten turbulenter kinetischer Energie beobachtet. Stark erhöhte Dissipationsraten wurden im gesamten Bereich von CW CE_2019_14N_25W, welcher in der Nähe der Insel Brava (Kap Verde) lokalisiert war, beobachtet. Die gemittelten Nitrat Flüsse aller Stationen mit weniger als 60 km Abstand zum Zentrum von CE_2019_18N_20W entsprechen $2.65 \times 10^{-2} \mu\text{mol m}^{-2} \text{s}^{-1}$. Die Stationen die zwischen 60 und 110 km vom Zentrum des Wirbels entfernt waren ergaben einen gemittelten Fluss von $8.98 \times 10^{-3} \mu\text{mol m}^{-2} \text{s}^{-1}$. Somit ist der Nitrat Fluss im Zentrum des Wirbels annähernd dreimal so stark wie außerhalb. Diese turbulenten Nitrat Flüsse sind unter den höchsten im offenen Ozean gemessenen Flüssen. Die stark erhöhte Turbulenz in CE_2019_14N_25W sorgte für einen Nitrat Fluss von $1.63 \times 10^{-1} \mu\text{mol m}^{-2} \text{s}^{-1}$. Ein Vergleich zwischen den Nitrat Flüssen und der gesamten Primärproduktionsrate (GPP), welche innerhalb der Wirbel bestimmt wurde, zeigte, dass die Nitrat Flüsse 13% der GPP innerhalb von CE_2019_18N_20W erhalten können. Die starken Nitrat Flüsse innerhalb von CE_2019_14N_25W decken 38% der dortigen GPP ab. Dies zeigt, dass die turbulente Nitrat Flüsse nicht den größten Beitrag zum Nährstoffbedarf der Primärproduktion innerhalb der Wirbel liefert.

Table of Contents

Abstract	1
Zusammenfassung	3
Table of Contents	5
1 Introduction.....	7
2 Data and Methods	11
2.1 Data.....	11
2.1.1 CTD-O ₂ / Nutrients profiles (CTD-profile)	11
2.1.2 Vessel mounted Acoustic Doppler Current Profiler (vmADCP)	12
2.1.3 Microstructure shear sensor (MSS) profiles	12
2.2 Turbulent kinetic energy dissipation	13
2.3 Vertical nutrient flux.....	14
2.3.1 Standard Error of fluxes	15
2.4 Conversion of dissolved oxygen into nitrate concentration.....	16
2.5 Velocity data analysis	16
2.5.1 Shear variance	16
3 Results	17
3.1 Conversion of AOU into nitrate concentration	17
3.2 Analysis of CE_2019_18N_20W	19
3.2.1 Distribution of turbulent kinetic energy dissipation	19
3.2.2 Turbulent nutrient fluxes.....	22
3.3 Comparison of CE_2019_18N_20W and CE_2019_14N_25W	27
4 Discussion	31
4.1 Sources of increased turbulence within the eddies	32
4.2 Impact on the ecosystem	35
5 References	37
6 Acknowledgements	43

1 Introduction

The global ocean represents an important component in the climate system, distributing heat and acting as a sink for CO₂ on a global scale (Landschützer et al., 2014). Ocean regions with strong carbon uptake capabilities are mostly associated with high biological production. In these areas, Carbon is fixed by photosynthesis during primary production. When the organic matter sinks into the interior of the ocean, it enables a vertical carbon pump (e.g. Ducklow et al., 2001). The export of organic matter also depletes the upper ocean layer of essential nutrients like nitrate, limiting the productivity to areas with vertical nutrient fluxes. In the open ocean, primary production is often associated with mesoscale features, on a horizontal scale, in the order of tens to hundreds of kilometers. Mesoscale nonlinear coherent vortices (hereafter referred to as eddies) represent an important and abundant feature in the world's oceans. In areas of weak background circulation, eddies can dominate the local velocity field (Chelton et al., 2011b).

Based on their vorticity, eddies are categorised into cyclonic eddies (CEs) with positive vorticity, rotating anticlockwise on the northern hemisphere, and anticyclonic eddies (ACEs) with negative vorticity, rotating clockwise on the northern hemisphere (Chelton et al., 2011b; Zhang et al., 2013; Schütte et al., 2016a). Eddy detection and characterisation can be achieved by remote sensing of sea surface height, where CEs (ACEs) are associated with depression (elevation) of the sea surface (e.g. Chelton et al., 2007; Schütte et al., 2016a). Considering the hydrographic aspects of the different eddy types, a third group of eddies can be identified. CEs show a doming of isopycnals and cold sea surface temperature (SST) in their core. Normal ACEs are identified by depression of isopycnals and warm SST in their core. However, some anticyclonic eddies host a thick lens of weakly stratified water, also known as a 'mode', within their core (Schütte et al., 2016a). This mode is often found within the main thermocline. Therefore, this third group of eddies is named anticyclonic mode water eddies (ACMEs) or intrathermocline eddies. ACMEs are not limited to the main thermocline, but can be found in all depth levels under a wide variety of names (e.g. Armi and Zenk, 1984). ACMEs are characterised by an upward displacement of isopycnals above the water lens leading to colder SST and a downward displacement below (Kostianoy and

Belkin, 1989; Karstensen et al., 2015). Showing only a weak elevation of the sea surface, ACMEs are difficult to track via remote sensing.

Due to their nonlinearity, eddies have the ability to isolate or trap water masses and ecosystems from the generation site inside their core, transporting them during their propagation over large distances and long time periods (Chelton et al., 2007; Karstensen et al., 2015; Schütte et al., 2016a). It has long been reported that eddies can form isolated hotspots of open ocean biological productivity that differ greatly from the surrounding, usually oligotrophic oceanic conditions (Menkes, 2002; McGillicuddy et al., 2007; Chelton et al., 2011a; Godø et al., 2012). This can influence the entire ecosystem from phytoplankton up to top predators (Tew Kai and Marsac, 2010). The relatively warm ACEs are usually unproductive (e.g. Palacios et al., 2006). In contrast, the cooler CEs and ACMEs establish a chlorophyll *a* maximum, associated with high primary production within their core (McGillicuddy et al., 2007; Goldthwait and Steinberg, 2008; Schütte et al., 2016b).

The eastern tropical North Atlantic (ETNA) with the eastern boundary upwelling system off the north-western African coast is one of the areas with the highest biological production in the world's oceans (Chavez and Messié, 2009; Lachkar and Gruber, 2012). Anomalies in this system can strongly influence local fisheries and economy. Schütte et al. (2016a) investigated the occurrence and characteristics of eddies in the ETNA, based on in-situ measurements and different satellite tracking algorithms. Depending on the tracking algorithm, they detected between 144 and 148 eddies per year with a lifetime of more than 7 days. 51-53% of the eddies were characterised as CEs, 38-40% as ACEs, and 9% as ACMEs. ACEs were found to have a slightly longer average and substantially longer maximum lifetime than CEs. This result is in agreement with other observational studies (Chaigneau et al., 2009; Chelton et al., 2011b) and theoretical predictions (Cushman-Roisin et al., 1990). The headlands of the African coast as well as the southwestern side of the Cap Verde islands have been found to be hotspots of eddy generation within the ETNA. From these generation sites, the eddies propagate with a speed of about 3 km day⁻¹ westward into the open ocean, with slight meridional deflections depending on the eddy type. During their propagation, the eddies transport the specific watermass-characteristics of the upwelling system

along with them. This abundance of eddies within the ETNA gives reason to suspect that they are of great importance in the local system (Schütte et al., 2016b).

During the propagation into the open ocean, CEs and ACMEs have been found to sustain their highly productive ecosystems, making them of great relevance for biogeochemical processes on a basin-wide scale (Oschlies and Garçon, 1998; Chelton et al., 2011a; Altabet et al., 2012; Stramma et al., 2013). Therefore, they have a great potential to contribute to the carbon fixation in the ocean. Karstensen et al. (2015) found a substantial decline in oxygen concentration closely below the mixed layer inside of CEs and ACMEs situated in the ETNA. Oxygen levels were found to decrease during the lifetime of the eddy, with respiration being three to five times higher than the normal background conditions. This suggests that biogeochemical processes and nonconservative water mass tracers are heavily impacted by individual eddies. Schütte et al. (2016b) found oxygen levels - in the ETNA - dropping below $10 \mu\text{mol kg}^{-1}$ in CEs and reaching suboxic levels of $<1 \mu\text{mol kg}^{-1}$ in ACMEs. The strong decrease in oxygen concentration in the subsurface layer strongly influences the marine ecosystem hosted by the eddy (Hauss et al., 2016).

To sustain the highly productive isolated ecosystems of the eddies in the surrounding oligotrophic open ocean, strong upward nutrient fluxes caused by physical processes are needed (Falkowski et al., 1991; McGillicuddy et al., 2007). McGillicuddy et al. (2007) found that the interaction between wind and eddies leads to positive (upwards) vertical velocities within ACMEs and negative vertical velocities inside CEs. This process alone leads to a negative impact on the productivity of CEs. Enhanced vertical nutrient fluxes into the mixed layer, induced by turbulent mixing inside the upper thermocline layer, are proposed to be a possible explanation for the enhanced primary production in CEs and ACMEs. Fer et al. (2018) found enhanced dissipation rates of turbulent kinetic energy per unit mass (ϵ), estimated from microstructure profiles in different parts of the Lofoten basin eddy, a long-lived anticyclone reaching depths of more than 2000 m. Fernández-Castro et al. (2020) analysed the flight path of a Seaglider to estimate ϵ in an ACME at the western boundary of the tropical north Atlantic. They found elevated dissipation rates ϵ at the base of the eddy core. Both studies proposed that the enhanced dissipation rates could be traced back to

interactions between the eddy and the internal wave field. Comparable studies in CEs are sparse.

In this study, two CEs situated within the ETNA (Figure 1) are analysed. The dissipation rates of turbulent kinetic energy, estimated from vertical microstructure profiles, are analysed to find hotspots of turbulent mixing. In addition, the irreversible vertical nutrient fluxes, caused by turbulent mixing, are calculated using nutrient profiles recorded in close temporal proximity at the site of the microstructure profiles. Thereby, this study strives to shed light on the mechanisms sustaining the highly productive ecosystems inside CEs by bringing nutrients to the euphotic layer. Since these ecosystems are strongly contributing to the productivity and carbon fixation of the open ocean, CEs are of high relevance for the global ecosystem and climate system.

2 Data and Methods

2.1 Data

As part of the REEBUS (Role of Eddies in the Carbon Pump of Eastern Boundary Upwelling Systems) project, an interdisciplinary research cruise to the ETNA on-board the research vessel Meteor - M160 - was conducted in 2019. M160 started on the 22nd of November and ended on the 20th of December. This study presents a part of the research data collected during this cruise. Two individual CEs were heavily sampled during the cruise using a wide range of devices. One of the sampled CEs was positioned north-east of the island Sal (Cape Verde) in the open ocean, which was named CE_2019_18N_20W. The other one was located south-west of the island Brava (Cape Verde), it revised the name CE_2019_14N_25W (Figure 1).

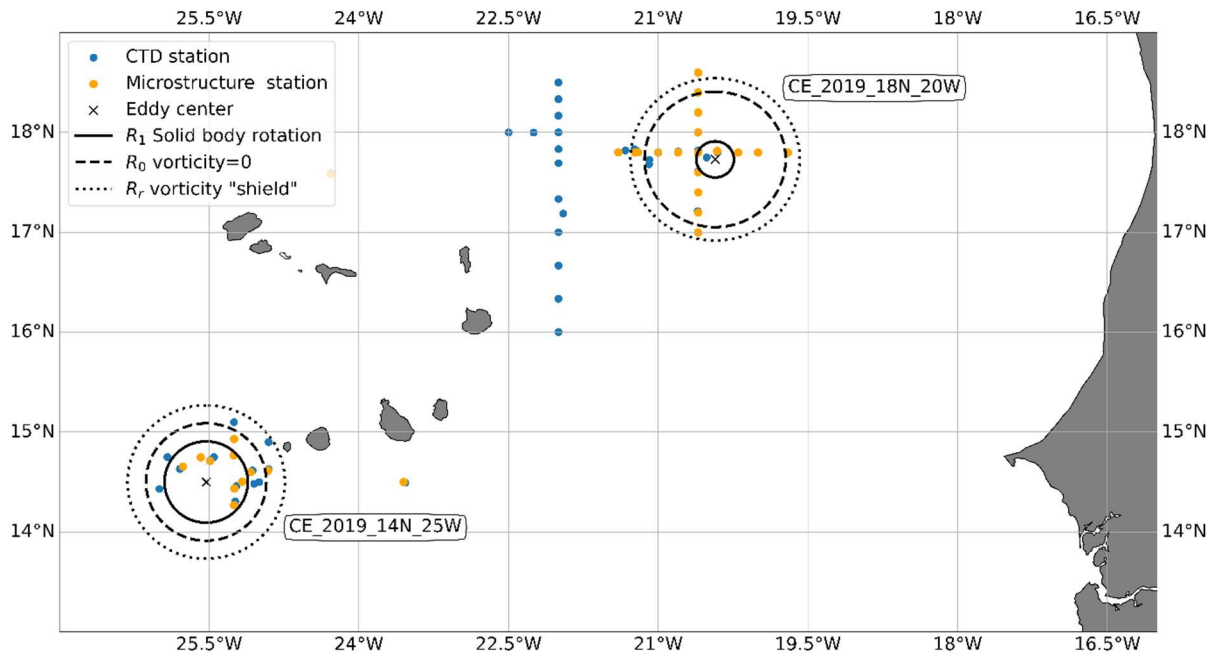


Figure 1: Map of the study area. The orange dots represent microstructure stations during M160. Blue dots indicate available CTD stations. The black cross marks the eddy center. The solid black line is the radius below which the fluid is in solid body rotation (R_0). The dashed black line represents the boundary of positive vorticity (R_0). The dotted black line is the outer limit of the negative vorticity "shield" (R_r) (Tim Fischer, personal communication).

2.1.1 CTD-O₂/ Nutrients profiles (CTD-profile)

During the cruises, 73 vertical profiles of conductivity (C), temperature (T), pressure (P), and dissolved oxygen (DO) were recorded using a Seabird Electronics (SBE) 9plus

system, attached to the water sampler carousel. Recent SBE Seasave software was used to record the data. Standard routines as well as visual inspection were used for post-processing. The profile data was averaged in 1 dBar bins. Water samples taken at discrete depth levels of the up-cast were used for the calibration of the conductivity and oxygen sensors following the recommendations of the Global Ocean Ship-Based Hydrographic Investigations Program (GO-SHIP) manual (Hood et al., 2010). For this purpose, a high-precision salinometer was used for conductivity calibration and Winkler titration was used for DO calibration. Discrete water samples were taken for the measurement of the nutrients nitrate, nitrite, phosphate, and silicate as well as several other parameters, which are not included in this study. In addition, numerous additional sensors were mounted to the water sampler carousel. From these, data of the OPUS UV spectral NO_x sensor (OPUS), measuring the combined concentration of nitrate and nitrite are used in this study. The OPUS was calibrated against the discrete water samples. A fully calibrated dataset was available for this study.

2.1.2 Vessel mounted Acoustic Doppler Current Profiler (vmADCP)

Post-processed current velocity data used in this study was recorded by the hull-mounted 75 kHz RDI Ocean Surveyor Acoustic Doppler Current Profiler of the research vessel Meteor. From the beginning of the cruise until the 12th December 2019, the vmADCP was configured to broadband mode with 8 m bin size. After the 12th December 2019, the vmADCP was reconfigured to 5 m bin size for the rest of the M160 cruise. Data is available for most of the cruise, with some minutes lost due to software issues. Instrument range was between 500 and 600 m. Current velocity data were averaged to 1 minute time intervals. During the cruise, the transducer misalignment angle was pre-set in the VmDAS Software used to record the data. Acceleration and deceleration close to stations were used as reference points during post-processing to correct the misalignment angle and amplitude factor (Fischer et al., 2003). In broadband mode with 8 m bin size, the standard deviation of 1-min-averaged velocity data from a 75 Hz vmADCP lies at about 0.03 m s⁻¹.

2.1.3 Microstructure shear sensor (MSS) profiles

A total number of 30 microstructure stations were recorded during the cruise. At each station, three repeated microstructure profiles were measured by a loosely tethered

MSS 90D microstructure profiler, manufactured by Sea&Sun Technology. Fall speed of the profiler was adjusted to 0.5 to 0.6 m s⁻¹. The MMS 90D was equipped with three individual airfoil shear probes, a fast thermistor, and a standard CTD unit. Airfoil shear probes and the fast thermistor record with a sampling rate of 1024 Hz, the CTD samples at 24 HZ. The microstructure profiler is capable of resolving the turbulent structure in the water column down to a cm scale. The profiles reach down to a depth of at least 200 m. At each station, a CTD-O₂ profile immediately preceded or followed the microstructure profiles. This study found an offset between the salinity measured by the conductivity cell of the MMS 90D and the conductivity cell of the SBE 9plus. A temperature dependency of the offset was found and was removed by a linear fit. Pressure and salinity dependencies were not found. As the SBE 9plus is calibrated against discrete water samples, the data of the MMS 90D was corrected to fit the data of the SBE 9plus.

2.2 Turbulent kinetic energy dissipation

The dissipation rate of turbulent kinetic energy (ε) is a measure of how much of the kinetic energy contained in the turbulent velocity field is transferred to heat via molecular friction. ε can be estimated by high-frequency velocity shear measured by airfoil probes (Osborn, 1974; Osborn, 1980; Oakey, 1982; Gregg, 1999; Schafstall et al., 2010). To compute dissipation rates, the shear variance method was used. Overlapping vertical intervals of 2 s - represented by 2048 individual measurements - were used for shear power spectrum calculation, resulting in a vertical resolution of 0.5-0.6 m. To derive estimates of ε , the relationship for isotropic turbulence was used to integrate the shear spectrum.

$$(1) \quad \varepsilon = 7.5\nu \overline{\left(\frac{\partial u}{\partial z}\right)^2} \approx 7.5\nu \left(\int_{k_{min}}^{k_{max}} E_{du'/dz}(k) dk \right)$$

Here, ν represents the kinematic viscosity of seawater. The shear wavenumber spectrum is represented by $E_{du'/dz}(k)$. k_{min} and k_{max} determine the integration boundaries wave numbers. For optimum accuracy, k_{min} and k_{max} are varied to include as much of the shear spectra as possible, while eliminating unwanted noise, e.g. from vibrations of the profiler. The upper boundary k_{max} increases with increasing dissipation rates (Moum et al., 1995). The spatial averaging caused by the size of the airfoil tip

results in a loss of variance, which was corrected using the methods described by Prandke and Stips (1998). To account for the loss of variance caused by incomplete integration, the wave spectrum was extrapolated using the Nasmyth spectrum (Nasmyth, 1970). After carefully editing the three individual estimates of ϵ for spikes - caused by collisions of the sensor with small objects - the three estimates were merged to a final estimate of ϵ . The fully processed and edited data was available for this study. Because the microstructure profiler needs to adjust its fall speed and because of ship-induced turbulence, the first 10 m of the profiles are not included in the study.

Gargett et al. (1984) showed that the assumption of isotropy is not always correct in the stratified ocean. In a strongly stratified fluid, the vertical turbulence is suppressed. In this case, equation (1) will overestimate the actual dissipation rate. As vertical fluxes are dominated by strong turbulent mixing events, the effects of anisotropy are neglected in this study.

2.3 Vertical nutrient flux

Turbulent mixing introduces an irreversible process acting against concentration gradients. In this study, turbulent nitrate fluxes into the mixed layer were estimated in the 10 dBar interval below the mixed layer depth (MLD) showing the strongest concentration gradient. In addition, mean flux profiles were generated using constant 15 dBar intervals. The MLD was set to the depth where the potential density was 0.125 kg m^{-3} higher than at a reference level of 6 dBar (Schafstall et al., 2010). The NO_x concentration gradient was at first derived from the data of the OPUS sensor. Given the high noise level of the OPUS sensor, this study opted to transform the data collected by the SBE oxygen sensor into nitrate concentrations (for details see section 2.4). To account for internal waves, vertically moving density surfaces between the individual profiles, the estimates of ϵ were retrieved from the MSS profiles in the same potential density interval as the potential density interval in the 10 dBar interval of the CTD profile.

To calculate vertical nutrient fluxes, the individual estimates of ϵ from the microstructure profiles were averaged for each station. The squared buoyancy frequency (N^2) - calculated from the CTD-profile immediately preceding or following the microstructure profiles according to equation (2) - and the averaged ϵ were used to calculate the turbulent eddy diffusivity (K_p) as in (3) (Osborn, 1980).

$$(2) \quad N^2 = -\frac{g}{\rho_0} \frac{d\rho}{dz}$$

$$(3) \quad K_p = \frac{\Gamma \varepsilon}{N^2}$$

Here, the mixing efficiency Γ was set to a constant value of 0.2 (Oakey, 1982), g represents the local gravity acceleration, ρ_0 is the mean potential density and $d\rho/dz$ represents the potential density gradient with depth.

Turbulent vertical fluxes F_c were calculated according to equation (4) from the turbulent eddy diffusivity (K_p) and the vertical concentration gradient ($\partial C/\partial z$). (Schafstall et al., 2010; Cushman-Roisin and Beckers, 2011)

$$(4) \quad F_c = K_p \frac{\partial C}{\partial z}$$

After careful visual inspection of all parameters, individual MSS profiles showing strong irregularities were excluded from the calculation.

2.3.1 Standard Error of fluxes

To obtain an evaluation of the uncertainties of the average turbulent eddy diffusivity and nutrient fluxes, a Gaussian error propagation was used as described by Schafstall et al. (2010).

$$(5) \quad \Delta K_p = K_p \left[\left(\frac{\Delta \Gamma}{\Gamma} \right)^2 + \left(\frac{\Delta \varepsilon}{\varepsilon} \right)^2 + \left(\frac{\Delta N^2}{N^2} \right)^2 \right]^{1/2}$$

Here, Δ represents the absolute uncertainties calculated for the averaged variables. In order to obtain a 95% confidence interval, ΔN^2 was calculated as two times the standard error. The standard error is defined as the standard deviation divided by the square root of the number of independent samples. As suggested by St. Laurent and Schmitt (1999), $\Delta \Gamma$ was set to a constant 0.04. To calculate the 95% confidence limits of ε , a bootstrap method described by Efron (1979) was used to account for the fact that ε does not follow a normal Gaussian distribution. The uncertainties of the nutrient fluxes were calculated in a likewise fashion.

$$(6) \quad \Delta F_c = F_c \left[\left(\frac{\Delta K_p}{K_p} \right)^2 + \left(\frac{\Delta \partial_z C}{\partial_z C} \right)^2 \right]^{1/2}$$

Here, $\Delta\partial_z C$ represents the doubled standard error of the vertical concentration gradient. This method does not account for systematic errors or measuring uncertainties. The total error may therefore be larger than calculated by this method.

2.4 Conversion of dissolved oxygen into nitrate concentration

Redfield (1934) found a close relationship between the respiration of oxygen and the nitrate concentration in seawater. To apply this relationship to the DO profiles, measured by the SBE Optode, the data from the discrete water samples were analysed. The Apparent oxygen utilisation (AOU) was used as a measure for the respiration of oxygen. AOU is defined according to (7) as the difference between the oxygen saturation at the surface ($O_{2,sat}$) and the measured DO concentration (Ito et al., 2004).

$$(7) \quad AOU = O_{2,sat} - DO$$

$O_{2,sat}$ was calculated following the methods of Weiss (1970). A least-square fit was used to establish a transformation polynomial. This transformation polynomial was subsequently applied to the AOU calculated from the CTD- O_2 data to calculate nitrate profiles.

2.5 Velocity data analysis

The velocity data recorded by the vmADCP were analysed to find the sources of the observed turbulence. Visual inspection of the data as well as the following calculations were used.

2.5.1 Shear variance

To gain an estimate of the activity of internal waves (IW), the shear variance (S^2) was computed from the vmADCP data according to (8) (Hummels et al., 2020).

$$(8) \quad S^2 = \left(\frac{du}{dz}\right)^2 + \left(\frac{dv}{dz}\right)^2$$

Here, du/dz and dv/dz represent the vertical gradient of the zonal and meridional velocity components respectively. High values of S^2 are an indicator for strong activities of IWs.

3 Results

3.1 Conversion of AOU into nitrate concentration

During the work on this study, it got apparent that the data quality of the OPUS sensor was rather poor. The noise level of the sensor is high, with a wave-like structure recognisable in the profiles (left panel Figure 2). This high noise resulted in high uncertainties in the calculation of concentration gradients. Furthermore, the OPUS sensor did not always properly record data, limiting the number of available profiles. The SEB oxygen sensor constantly measured data with a significantly lower noise level than the OPUS sensor. The comparison of AOU and nitrate concentration derived from water samples showed a close correlation between the two parameters (right panel Figure 2). Nitrite concentrations were small and not always measured at the same depths as oxygen and nitrate, therefore nitrite was not included in the transformation. The second-order polynomial, calculated by a least-square method, showed the highest agreement with the available data in the first 600 dBar of the water column. The comparison of the results of the transformation to the data of the OPUS sensor and the water samples shows that the results of the transformed nitrate concentrations are generally higher than the measurements of the OPUS sensor (left panel Figure 2). At the same time, the concentrations derived from the AOU transformation well agree with the water samples. As the OPUS sensor measures the combined concentration of nitrate and nitrite it should show higher concentrations than the transformation that only considers nitrate. Due to the significantly reduced noise level of the transformed nitrate profiles, concentration gradients calculated from these profiles have strongly reduced uncertainties, especially in regions that show small concentration gradients. Therefore, the second-order transformation equation was used for all further calculations within this study.

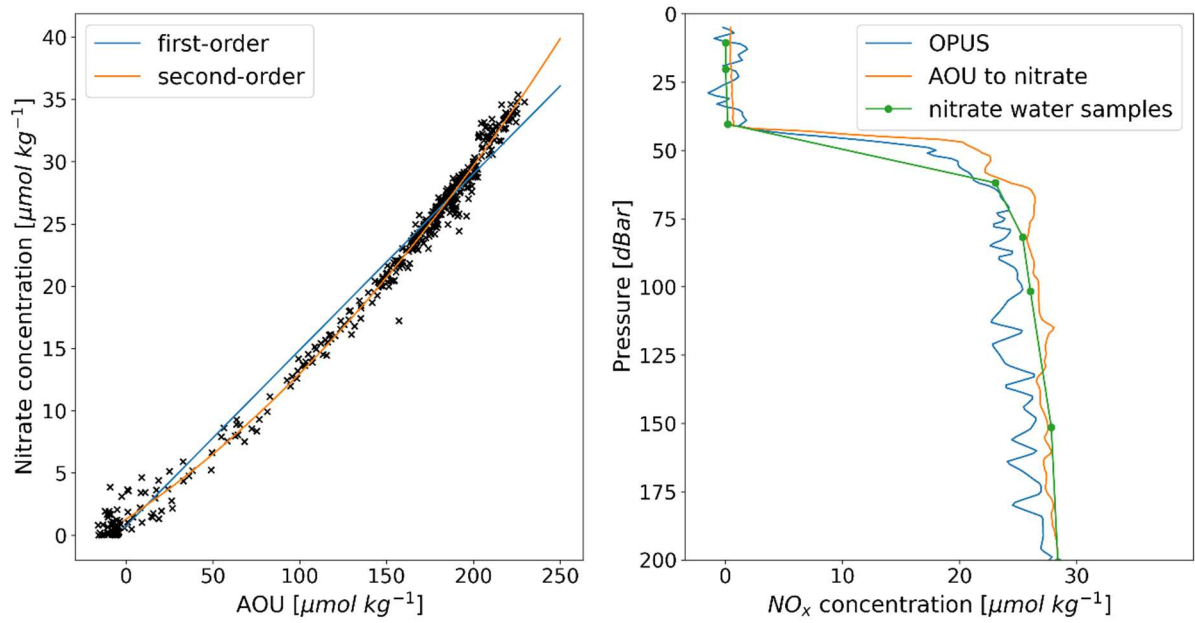


Figure 2: Transformation of AOU to nitrate. The left panel shows the distribution of all discrete water samples above 600 dBar marked by a black “x”. The blue line represents the first-order least-square fit. The orange line indicates the second-order polynomial. The panel on the right shows the profile recorded at CTD station 36. The blue line displays the data of the Opus sensor. The orange line indicates the result of the AOU transformation. The green line shows the values of discrete water samples. Green dots mark the individual samples.

3.2 Analysis of CE_2019_18N_20W

This study analysed data of two individual CEs in the ETNA. As CE_2019_18N_20W was situated in the open ocean, far away from interactions with topography, it was assumed to be a good candidate for a representative CE within the ETNA (Figure 1). Furthermore, the sampling strategy used with two clear crosssections enabled a clear assessment of the eddy. Therefore, CE_2019_18N_20W was first and most intensely analysed.

3.2.1 Distribution of turbulent kinetic energy dissipation

The first assessment of the available data indicated that CE_2019_18N_20W shows typical features associated with a CE. The isopycnals show the typical doming towards the CEs center, as observed by other studies (e.g. Schütte et al., 2016a). Assuming that the eddy is in a cyclogeostrophic balance, the doming isopycnals result in a cyclonic rotation. This cyclonic rotation is also evident in the velocity data of the vmADCP (not shown). Following the doming isopycnals, the mixed layer shallows towards the center (Figure 3). The water in the mixed layer within the center of the eddy is cooler, less saline, and denser than in the outer parts of the eddy. The doming isopycnals and shallow MLD lift the nutrient-rich water from the ocean interior closer to the surface. This process can be considered as a preconditioning for elevated nutrient fluxes into the mixed layer. High dissipation rates are observed throughout the highly energetic wind-driven mixed layer. As the mixed layer is weakly stratified, or even unstratified, no estimates of the impact of turbulence on watermass properties and nutrient distribution can be made. Therefore, the mixed layer is excluded from all further considerations. Below the mixed layer, dissipation rates show a high variability on small vertical and horizontal scales (Figure 3). Variations over several orders of magnitude between neighbouring stations or even within a single profile are a common feature of the turbulent velocity field. As these variations can also accrue on small temporal scales, it is always necessary to record and average multiple stations with multiple repeated profiles to gain a robust estimate of the turbulent structure. The highest dissipation rates below the mixed layer are observed in the center of the eddy closely below the mixed layer, reaching values around 10^{-6} W m^{-2} (Figure 3).

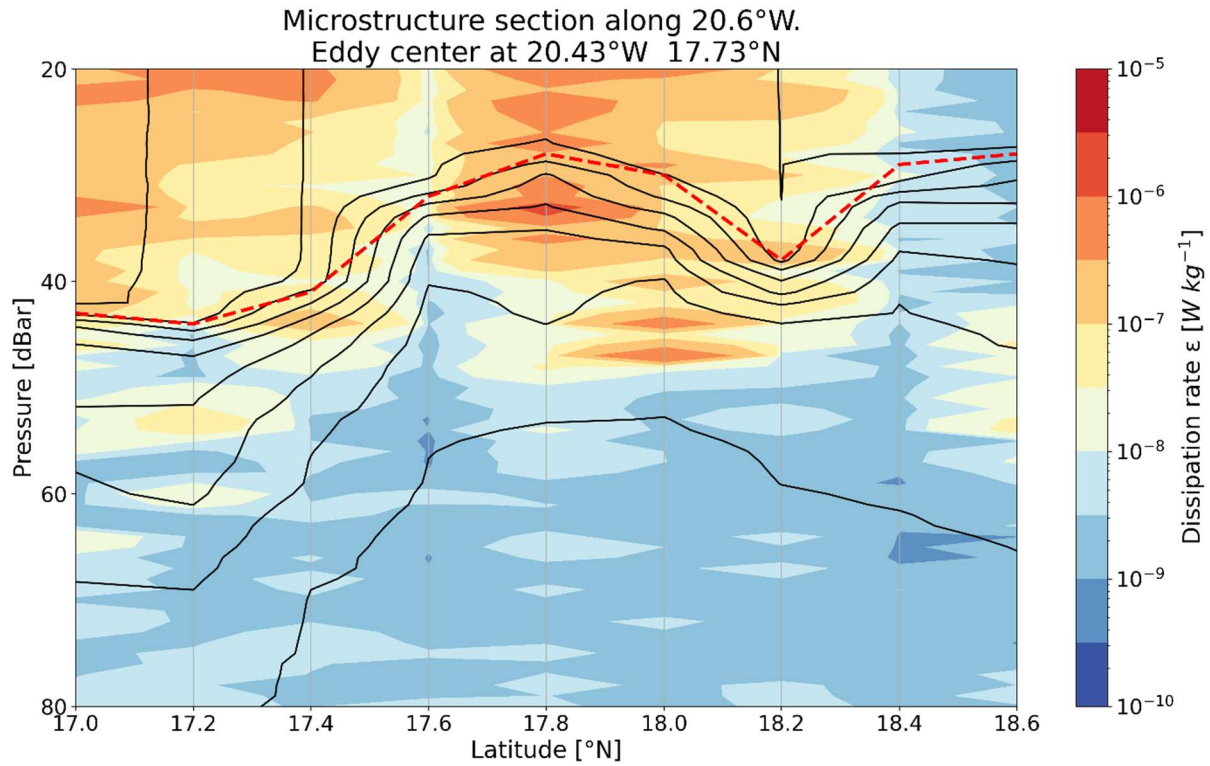


Figure 3: Meridional microstructure section of CE_2019_18N_20W along 20.6°W. The estimates of the dissipation rate ϵ , displayed by filled contours, from the individual profiles were averaged for each station. The solid black lines represent potential density anomaly σ [kg m^{-3}] contours, spaced at 0.2 kg m^{-3} intervals. The dashed red line displays the MLD. The grey vertical grid lines, as well as the left and right edge, indicate the positions of MSS Stations.

To gain a better understanding of the turbulent structure of the eddy, all 18 stations recorded in the proximity of CE_2019_18N_20W are referenced according to their distance from the eddy center. Tim Fischer (personal communication) calculated the center position of CE_2019_18N_20W and CE_2019_14N_25W as well as three characteristic radii (see Figure 1) during a close examination of the vmADCP data. The composite of all stations sorted by distance from the eddy center confirms the first impression of the eddy structure. Highest dissipation rates are observed in the center of the eddy accumulating near the mixed layer. More than 20 dBar below the MLD, ϵ rarely exceeds 10^{-8} W m^{-2} throughout the entire eddy (Figure 4). To compare the individual stations with each other, the ϵ values were integrated from the MLD to 80 dBar below the MLD. As the dissipation rates in the lower levels are very small, the results of the integration do not significantly change when the lower integration boundary moves to deeper or higher levels. Integrated dissipation rates increase towards the center of the eddy, with strong fluctuations between stations (Figure 4). The average over the nine stations with less than 60 km distance from the center results in a vertically integrated ϵ of $1.03 (0.80 - 1.24) \text{ mW m}^{-2}$. Values in brackets

display the lower and upper boundaries of a 95% confidence interval determined by a bootstrap method. Averaging the nine stations with more than 60 km distance from the center results in 0.51 ($0.44 - 0.58$) mW m^{-2} . This indicates about twice as much turbulent dissipation inside the eddy than outside. As the 95% confidence intervals of the two estimates do not overlap, the increase in dissipation rates towards the center is significant. During the observation, CE_2019_18N_20W was very weak with an inner core radius R_1 of only 20 km. Therefore, only a single station was within the inner core, a second station was situated just outside the core radius. Even if both stations were assigned to the inner core and averaged accordingly, the result would not be a robust estimate, since it would be based on insufficient data. Consequently, this work does not further separate the eddy into smaller parts.

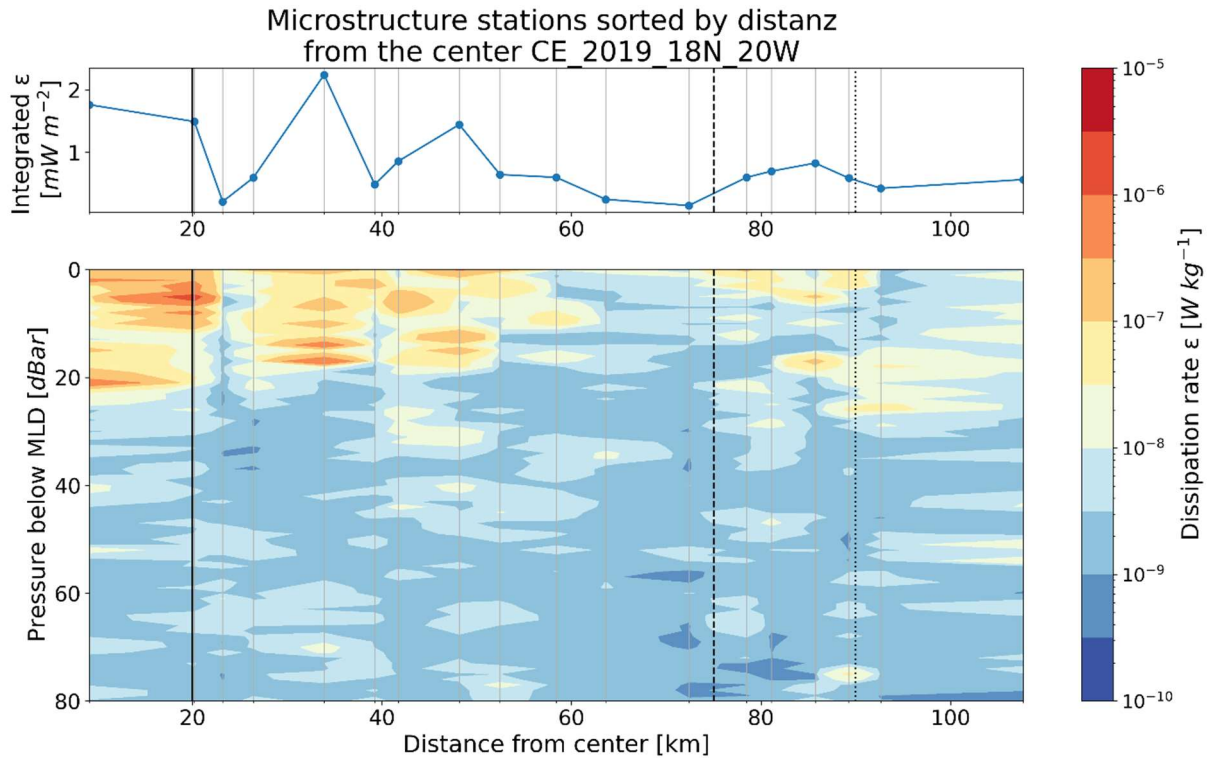


Figure 4: Composite of all MSS stations available in the proximity of CE_2019_18N_20W sorted by distance from the eddy center. The top panel shows the vertically integrated dissipation rates from the MLD to 80 Meters below the MLD. The bottom panel shows the station averaged estimates of ϵ below the MLD, displayed by filled contours. The grey gridlines indicate the position of the individual MSS stations. The solid black line represents R_1 . The dashed black line displays R_1 . And the dotted black line indicates R_r .

3.2.2 Turbulent nutrient fluxes

A wide variety of biological, chemical as well as physical mechanisms control the vertical distribution of nutrients - such as nitrate (NO_3^-) and nitrite (NO_2^-) - in the water column. When light is abundant, as is the case in the ETNA, primary production quickly consumes all available nutrients within the euphotic zone (Lévy et al., 2012). In this case, vertical nutrient supply into as well as the remineralisation rate within the euphotic zone are limiting factors for primary production. There are different approaches to determine the vertical turbulent nutrient flux into the euphotic zone. Numerous studies have used the nutrient gradient just below the mixed layer to determine the nutrient flux into the euphotic zone (e.g. Schafstall et al., 2010). Other studies used the interval below the mixed layer showing the strongest concentration gradient (e.g. Hales et al., 2005). This study uses the second approach, as the biological nutrient consumption is likely to be highest where the strongest concentration gradient is located. Considering this, the flux across this gradient will have the strongest impact on the primary production and the following ecosystem. Inspecting the data of CE_2019_18N_20W, it is apparent that the strongest vertical nutrient gradient and the mixed layer base are mostly in the same position (Figure 5). Nitrate concentrations in the mixed layer are close to zero indicating an oligotrophic environment in the surface waters. Below the MLD, nitrate concentrations rapidly increase to around $25 \mu\text{mol kg}^{-1}$, with only a few stations showing low concentrations below the MLD.

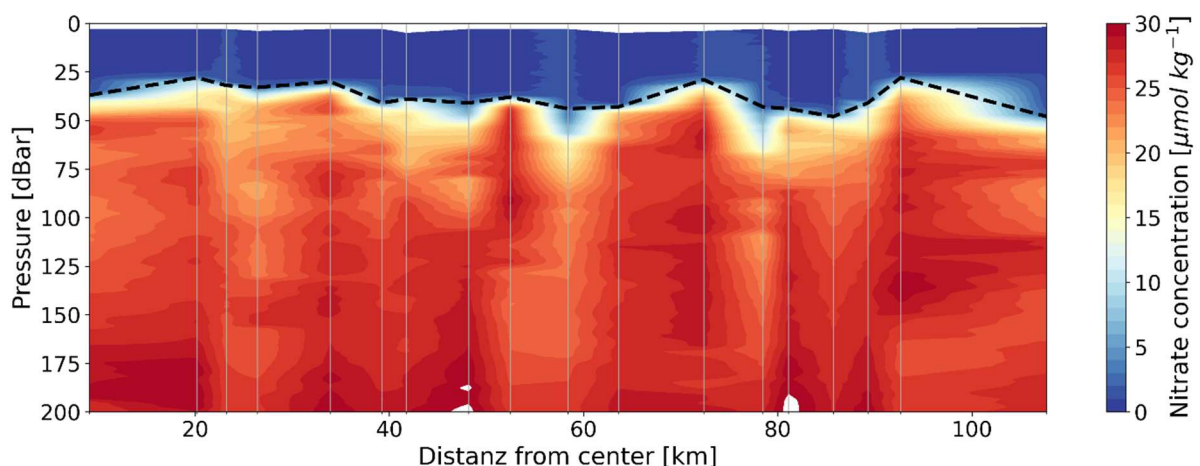


Figure 5: Nitrate distribution sorted by distance from the center of CE_2019_18N_20W. The grey gridlines as well as the left and right edge represent the positions of individual stations. The black dashed line indicates the MLD.

The turbulent nitrate fluxes calculated for the 18 stations in the proximity of CE_2019_18N_20W show strong fluctuations between individual stations (Figure 6). These fluctuations are in general agreement with the distribution of dissipation rates presented in Section 3.2.1. The nitrate fluxes increase towards the center of the eddy. Using the same averaging intervals as before, the inner nine stations result in an average vertical nitrate flux of $2.65 (2.13 - 3.08) \times 10^{-2} \mu\text{mol m}^{-2} \text{s}^{-1}$. The nine stations with more than 60 km distance from the eddy center average to $8.98 (6.74 - 9.20) \times 10^{-3} \mu\text{mol m}^{-2} \text{s}^{-1}$. Values in brackets represent the lower and upper boundary of the 95% confidence interval, calculated by error propagation. This indicates an almost 3 times higher vertical nitrate flux in the inner 60 km of the eddy than compared to the nine stations with more than 60 km distance to the center of the eddy

To evaluate the quality of the microstructure data used for the flux calculation, the distribution of the individual estimates of ϵ was analysed. The flux estimate for the nine stations closer than 60 km to the center of the eddy is based upon 518 individual estimates of ϵ . The nitrate flux estimate of the stations with more than 60 km distance from the eddy center was determined using 353 individual estimates of ϵ . The large difference in the number of individual estimates results from excluding two profiles, which show very strong irregularities from the calculation. The ϵ estimates show a logarithmic distribution, a common characteristic of the turbulent field (Figure 7). The distribution of the inner nine stations is shifted towards higher dissipation rates,

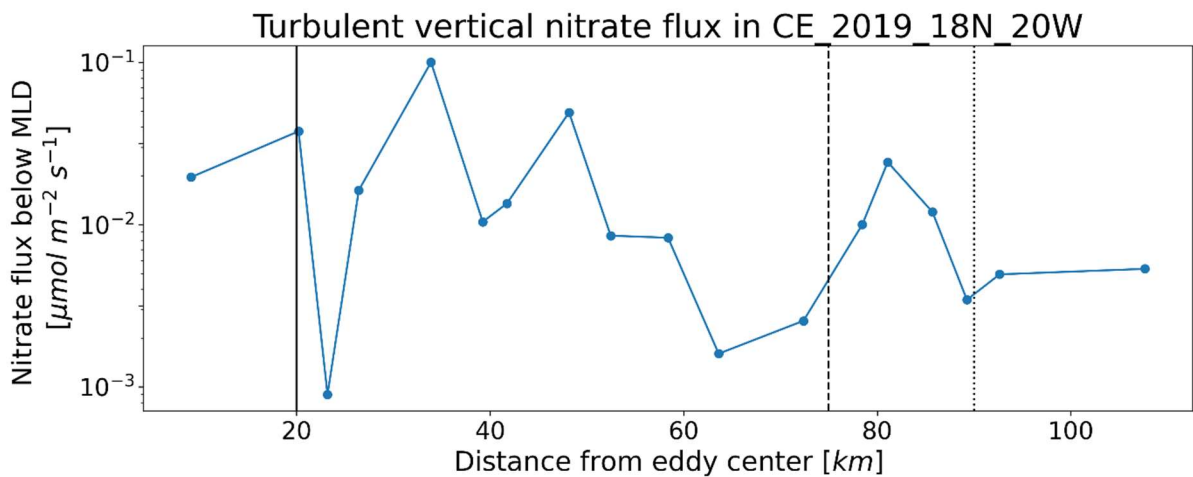


Figure 6: Turbulent vertical nitrate fluxes displayed by distance to the center of CE_2019_18N_20W. The solid black line indicates R_1 . The dashed black line represents R_1 . And the dotted black line displays R_r .

compared to the distribution of the stations with more than 60 km distance from the eddy center. This is in agreement with the higher integrated dissipation rates found within the eddy. No individual estimate of ϵ is found that strongly exceeds the rest. The depth interval, between 180 and 190 dBar, close to the lower end of the profiles was used as a reference distribution. The interval shows low dissipation rates, therefore, the distribution is considered as the distribution of background noise. Comparing the distribution in the interval showing the strongest vertical nitrate gradient with the background conditions between 180 and 190 dBar, a strong shift towards high dissipation rates is observed for the interval in which the nitrate flux was calculated (Figure 7). This indicates that strong signals are recorded in the flux calculation interval, which are only weakly influenced by the instrument noise level. Considering the number of individual estimates as well as the well-defined distribution, the dissipation rates used for the calculation of the turbulent nitrate flux are based on good quality data and therefore delivers a robust estimate.

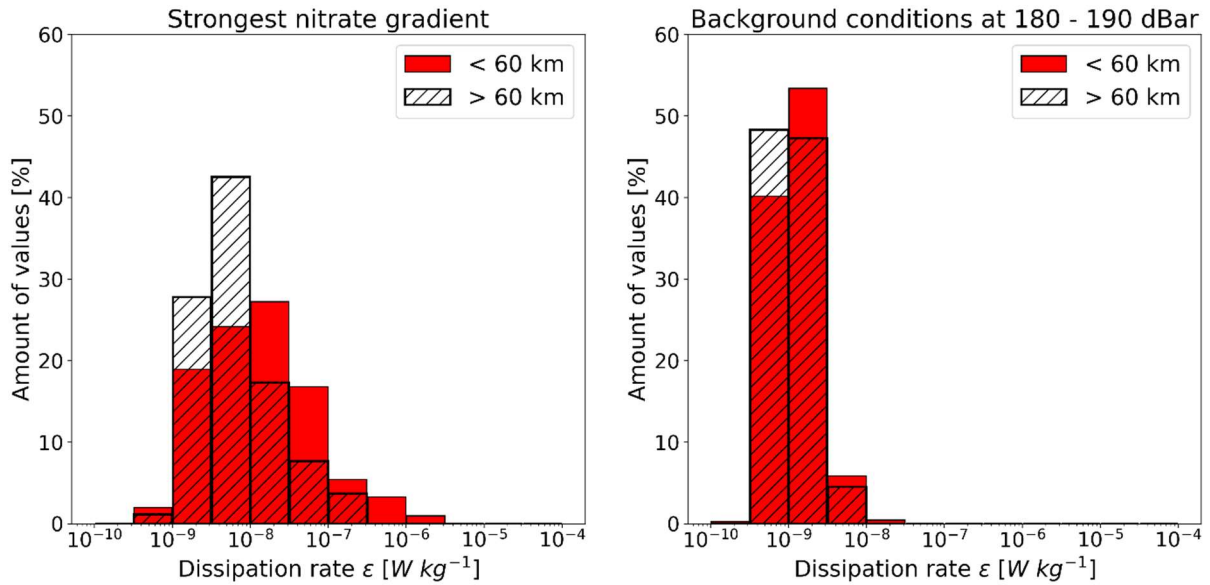


Figure 7: Logarithmic-spaced histogram of the individual estimates of dissipation rate ϵ within CE_2019_18N_20W. The left panel shows the distribution in the 10 dBar interval with the strongest nitrate concentration gradient. The right panel displays the distribution between 180 and 190 dBar. The stations with less than 60 km distance to eddy center are shown by the red bars. The back striped bars represent the stations with more than 60 km distance to the eddy center.

Analysing the other parameters contributing to the vertical flux calculation, it is not possible to find a significant difference between the inner and outer stations. The vertical nitrate concentration gradient calculated for the inner nine stations is $1.49 \pm 0.33 \mu\text{mol L}^{-1} \text{ m}^{-1}$ (\pm denotes the 95% error band). The nine stations with more than 60km distance to the eddy center show a concentration gradient of $1.46 \pm 0.25 \mu\text{mol L}^{-1} \text{ m}^{-1}$. The differences in the buoyancy frequency were likewise insignificant.

The mean flux profiles displayed in Figure 8 provide insights into the origin of the nitrate transported into the mixed layer. It can be seen that the strong stratification just below the mixed layer counteracts the higher dissipation rates leading to slightly increasing eddy diffusivities with increasing depth in both areas, being less pronounced for the inner nine stations. For the inner nine stations, the vertical nitrate concentration gradient shows a very pronounced divergence between the first and second interval, dropping from gradients around $1 \mu\text{mol L}^{-1} \text{ m}^{-1}$ to values close to zero. This divergence can also be found in the outer nine stations but is not as pronounced. Here, the concentration gradient decreases from around $1 \mu\text{mol L}^{-1} \text{ m}^{-1}$ to values around $0.4 \mu\text{mol L}^{-1} \text{ m}^{-1}$. For the inner nine stations, strong upward nutrient fluxes within the interval from the mixed layer to 15 dBar below the mixed layer can be observed. Below this, the average flux decreases by an order of magnitude, and the uncertainties in the flux become large. Sometimes negative (downward) fluxes are observed. The flux divergence between the first and second interval indicates that the nitrate transported into the mixed layer by turbulent fluxes mainly originates in the waters just below the mixed layer. In the outer nine stations, this divergence is not as prominent. Uncertainties in the mean flux become very large below 30 dBar indicating that the nitrate transported into the surface originates from the first 30 dBar below the MLD.

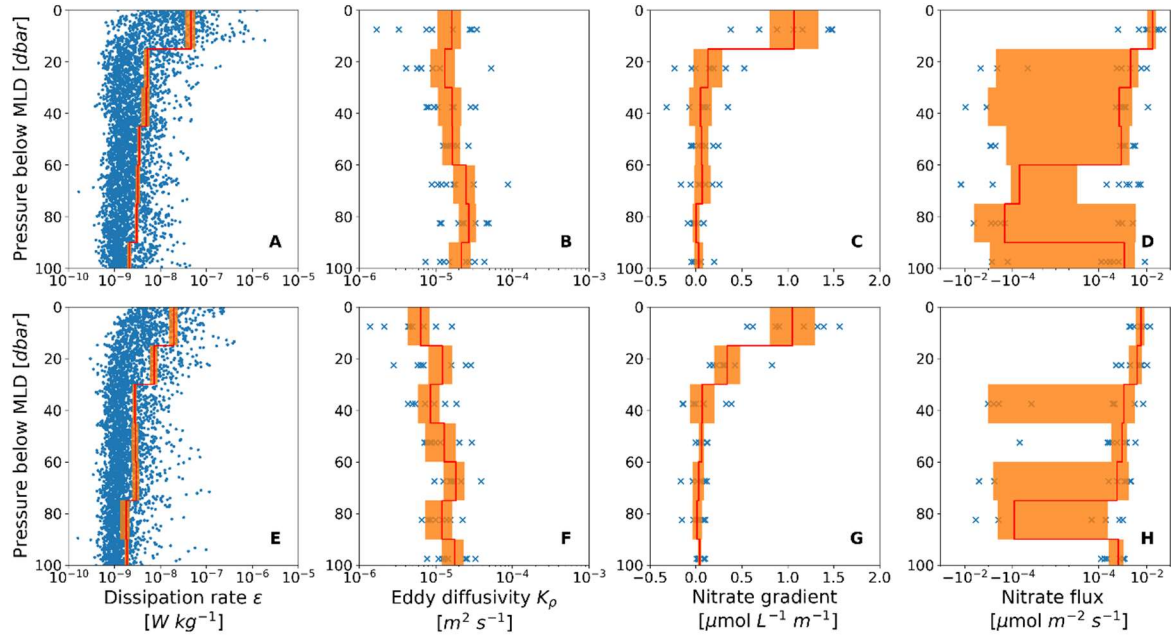


Figure 8: Mean profiles of all parameters contributing to the vertical nitrate flux within CE_2019_18N_20W. The top row (panels A - D) represent the nine stations with less than 60 km distance to the center. The bottom row (panels E - H) display the nine stations with more than 60 km distance from the eddy center. The blue dots in A and E represent the individual estimates of ϵ . The blue (x) in B - D and F - H show the individual estimates from the stations. The red line displays the interval mean. The orange areas indicate a 95% confidence interval.

3.3 Comparison of CE_2019_18N_20W and CE_2019_14N_25W

The eddy CE_2019_14N_25W was detected very close to the Cape Verde archipelago and was sampled two times during the M160 cruise. The analysed microstructure profiles were recorded during the second visit. From a close inspection of the vmADCP data, it was apparent that the eddy had strongly changed its shape to an elliptical form between the two sampling periods. This results in great uncertainties in the position of the eddy center as well as the characteristic radii (Tim Fischer, personal communication). Therefore all nine MSS Stations in the proximity of CE_2019_14N_25W were assumed to be within the eddy and analysed as a whole.

The observed dissipation rates within the eddy were very high ($\sim 10^{-7} \text{ W kg}^{-1}$), with high values found in greater depths below the mixed layer (Figure 9). This represents a contrast to CE_2019_18N_20W, where dissipation rates more than 20 dBar below the MLD were seldom higher than $10^{-8} \text{ W kg}^{-1}$. The distance from the eddy center given in

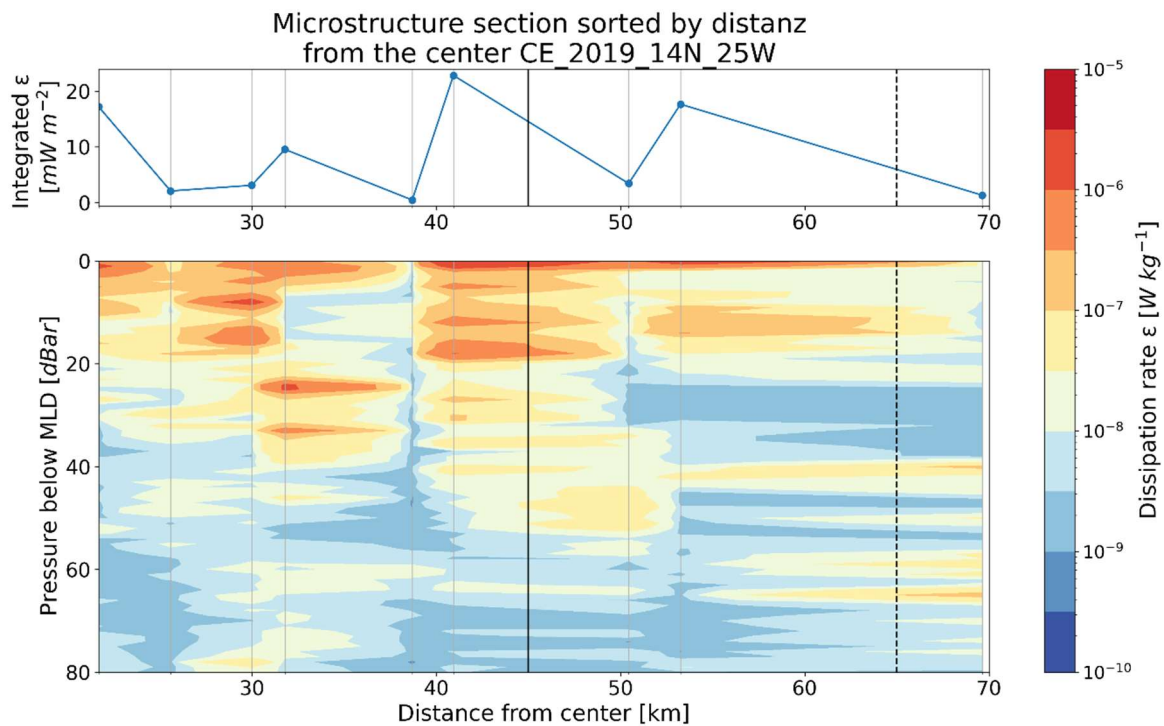


Figure 9: Composite of all MSS stations available in the proximity of CE_2019_14N_25W. The distance from the center on the x-axis has to be handled with care, serving mainly for means of display. The top panel shows the vertically integrated dissipations rates from the MLD to 80 Meters below the MLD. The bottom panel shows the averaged estimates of ϵ below the MLD, displayed by filled contours. The grey gridlines indicate the position of the individual MSS stations. The solid black line represents R1. The dashed black line displays R1.

Figure 9 has to be handled with great care and serves only as a rough indicator to display the stations. Vertical integration and averaging of the dissipation rates between the MLD and 80 dBar below the MLD for all stations results in $8.62 (6.75 - 10.24) \text{ mW m}^{-2}$, the values in brackets represent the 95% confidence interval. This indicates almost 17 times more turbulent kinetic energy dissipation for the nine stations within CE_2019_14N_25W than estimated for the nine stations with more than 60 km distance to the center of CE_2019_18N_20W.

The nitrate distribution within CE_2019_14N_25W shows prominent differences to CE_2019_18N_20W (Figure 5, Figure 10). Low nitrate concentrations are observed in deeper layers below the mixed layer. The transition from low to high nitrate concentrations stretches over a much longer depth interval than in CE_2019_18N_20W, where a very steep gradient just below the MLD can be observed. The observed nitrate concentrations at 200 dBar are almost equal in both eddies.

The highly elevated turbulence within CE_2019_14N_25W directly impacts the vertical nitrate flux below the mixed layer. The average nitrate flux of all stations together is $1.63 (1.38 - 1.84) \times 10^{-1} \mu\text{mol m}^{-2} \text{ s}^{-1}$, which estimates 20 times higher nitrate flux than averaged for the outer nine stations of CE_2019_18N_20W. The significant difference in the turbulent structure can also be observed in the distribution of dissipation rates

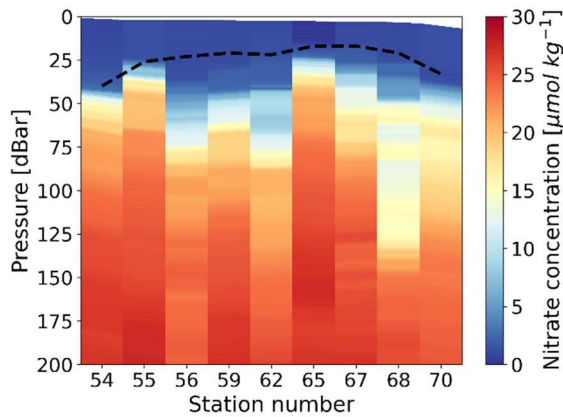


Figure 10: Nutrient distribution within CE_2019_14N_25W displayed by the CTD station number. The solid black line indicates the MLD. Note that the station number does not indicate the position within the eddy.

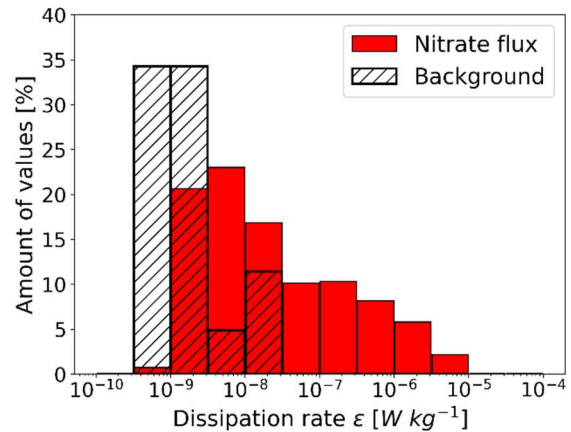


Figure 11: Logarithmic-spaced histogram of the distribution of ϵ within CE_2019_14N_25W. The red bars shows the distribution in the 10 dBar interval with the strongest nitrate concentration gradient. The black striped bars displays the distribution between 180 and 190 dBar.

used for the flux calculation (Figure 11). The distribution is heavily shifted towards higher dissipation rates with a maximum near $10^{-7} \text{ W kg}^{-1}$. Even in the interval between 180 and 190 dBar, dissipation rates of more than $10^{-8} \text{ W kg}^{-1}$ were found. With $0.81 \pm 0.10 \mu\text{mol L}^{-1} \text{ m}^{-1}$, the maximum concentration gradient for which the nitrate flux was calculated is significantly weaker than observed in CE_2019_18N_20W. The same is true for the stratification, represented by N^2 , which is lower in CE_2019_14N_25W. Unlike in CE_2019_18N_20W, the strongest concentration gradient and the mixed layer base are not as closely linked within CE_2019_14N_25W. This indicates that high biological consumption is present below the mixed layer.

Strong differences between the two eddies are found by analysing the mean profiles of all parameters contributing to the nitrate flux (Figure 8, Figure 12). The highly increased dissipation rates and the weaker N^2 (not shown) lead to high eddy diffusivities in the upper intervals of CE_2019_14N_25W decreasing with depth, in contrast to K_p in CE_2019_18N_20W. Furthermore, the eddy diffusivities in CE_2019_14N_25W show a broader range between individual stations, pronouncing the higher variability of CE_2019_14N_25W. The high nitrate concentration gradients as well as significant step between the first and second interval observed in CE_2019_18N_20W, cannot be found within CE_2019_14N_25W. Here the gradient is weaker and rather constant over the first 30 dBar below the mixed layer. The common feature of both eddies is the divergence in the nitrate flux in the upper intervals. This indicates that the nitrate transported into the mixed layer originates mainly in the waters directly below the mixed layer despite the strongly differencing parameters within the two eddies.

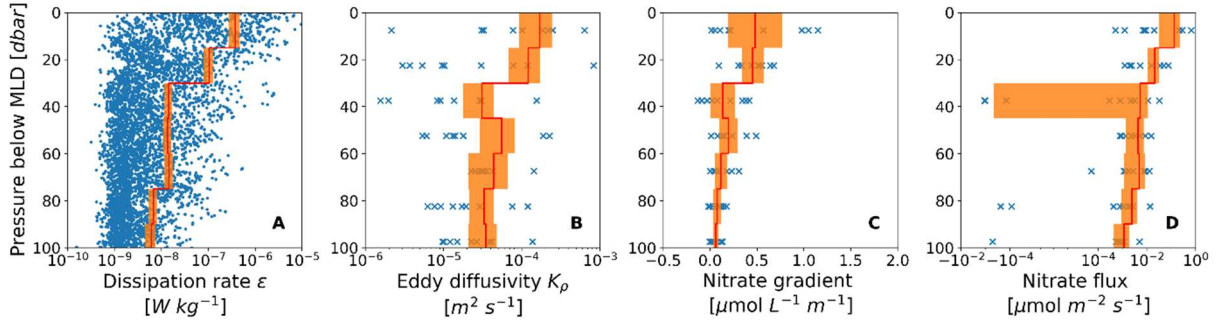


Figure 12: Mean profiles of the parameters contributing to the vertical nitrate flux within CE_2019_14N_25W. The blue dots in A represent the individual estimates of ϵ . The blue (x) in B - D highlight the individual estimates from the stations. The red line displays the interval mean. The orange areas indicate a 95% confidence interval.

4 Discussion

This study investigated the turbulent structure and nitrate fluxes of two CEs situated within the ETNA. Thereby, this study aimed to find hotspots of increased turbulent mixing and nitrate transport associated with the mesoscale feature, which would provide an explanation for the increased primary production within CEs. Using the available microstructure data, this study found a significant increase in the dissipation rates of turbulent kinetic energy within the two observed CEs. Due to the high variability of dissipation rates on small spatial and temporal scales, the estimates are influenced by uncertainties that are usually larger than presented by the statistical evaluation. The strong peak near 58 dBar in profile MSS 1 in panel B of Figure 14 could also have been interpreted as a malfunction of the instrument. If this profile was excluded from the calculation, the result might be different. As the turbulent field is not constant in time, rare but strong mixing events dominate the mean fluxes. The importance to determine the frequency of these strong events emphasises the need to combine multiple stations and profiles to form a robust estimate. As this study evaluated 27 MSS stations with 81 individual profiles, the results presented here can be considered as a good estimate, especially with the well-defined distribution of dissipation rates presented in section 3. The data from a second cruise - M156 -, conducted as part of the REEBUS project, where a third CE was heavily sampled, became available near the end of this work. Due to multiple irregularities in the dataset, it was no longer possible to include the observations in this work. This dataset can be used to extend the results of this work. To further widen the dataset it would be possible to reference all available MSS profiles recorded during different cruises to an eddy tracking algorithm. A procedure like this was used by Schütte et al. (2016a) to gain valuable insights on the average distribution of hydrographic parameters within the different types of eddies. Applying this approach to the MSS profiles would substantially increase the number of available profiles, largely improving the quality of the results. Furthermore, this approach would gain insights into the turbulent structure within the different types of eddies, not only CEs.

4.1 Sources of increased turbulence within the eddies

The vmADCP velocity data was partly analysed to gain insights into the origin of the increased turbulence within the two observed eddies, but further research has to be conducted for a deeper understanding. The shear variance S^2 increases towards the center of CE_2019_18N_20W (Figure 13). The large-scale effect of the rotation of the eddy could potentially lead to regions of increased S^2 . If this was the case, the S^2 signal would be relatively constant over time. By visualising all station parameters, increased levels of S^2 are observed within the main thermocline (Panel C Figure 14). The water velocities show strong variations on small time scales, indicating high activity of internal waves (Panel D, E Figure 14). The strong vertical displacement of the thermocline between the CTD profile and the MSS profiles seen in panel A of Figure 14 also indicates the high activity of internal wave with high frequencies.

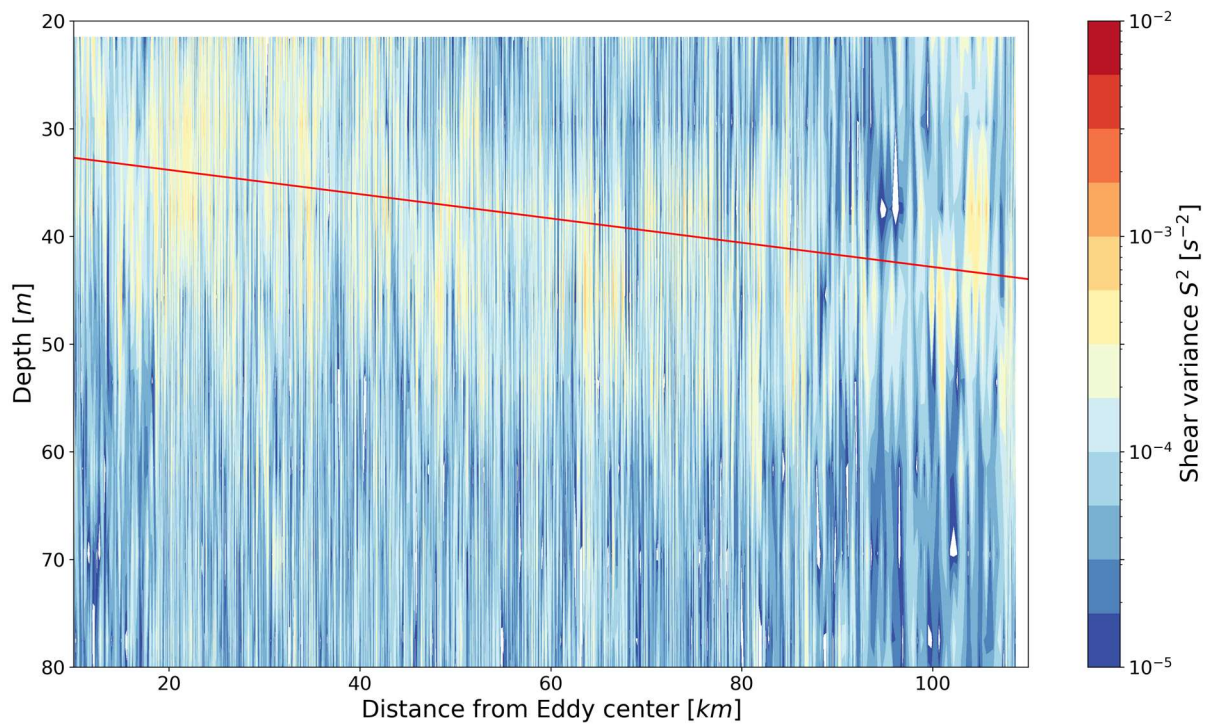


Figure 13: Shear variance S^2 calculated from the data of the vmADCP sorted by distance to the center of CE_2019_18N_20W. The red line displays the position of the MLD estimated by linear regression.

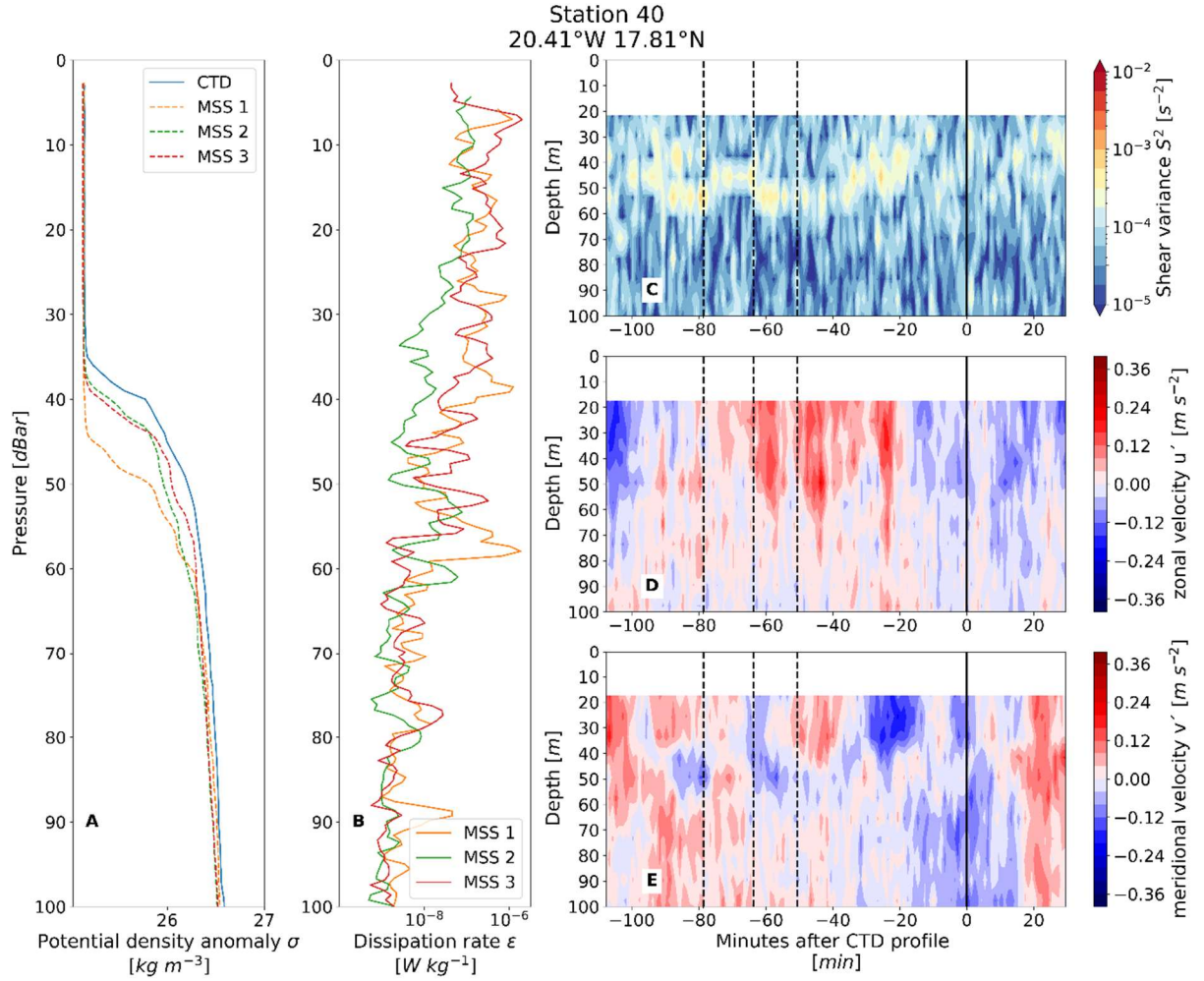


Figure 14: Hydrographic, microstructure, and velocity data of station 40 close to the center of CE_2019_18N_20W. Panel A shows the potential density anomaly σ profiles. B displays the dissipation rates of the three MSS profiles taken at this station. C shows the shear variance S^2 calculated between the depth bins of the vmADCP data. Panels D and E display the time varying components of zonal velocity u' and meridional velocity v' respectively, generated by removing the station mean velocity from the data.

This study did not further investigate the sources of increased turbulence found within the two observed CEs. A deeper study of the observed data as well as theoretical and numerical studies could substantially contribute to the understanding of the mechanisms governing the turbulent system of the eddy. Using an idealised numerical model of baroclinic unstable flows, Chouksey et al. (2018) found an increase in the emission of internal gravity waves (IGW) in flows with a large Rossby number (Ro). Ro is defined as $Ro = \frac{U}{Lf}$, where U is the characteristic velocity, L is the characteristic length scale, and f is the local Coriolis parameter. This implies that eddies with a high

rotation velocity generate more IGW. The downscale energy cascade of these IGW leads to increased dissipation rates. Applying raytracing simulations on idealised as well as the observed velocity fields of eddies would lead to a better understanding of the dissipative pathways of the internal waves in and around eddies (Olbers and Eden, 2017). The generation of a wave power spectrum in and around the Eddies could facilitate a more detailed insight of the internal wave field. Löb et al. (2020) found strong interactions between internal tides and mesoscale eddies, potentially transferring tidal energy into turbulent dissipation. As tidal interactions might increase in the proximity of topography, such as the Cape Verde islands, this could partly explain the highly increased dissipation rates observed in CE_2019_14N_25W. Detailed investigation of the interaction of the mean eddy flow with the topography of the islands as well as the strong deformation CE_2019_14N_25W experienced during the M160 can potentially enhance the understanding of the sources of observed turbulence.

4.2 Impact on the ecosystem

With the available dataset, this work was able to estimate the turbulent vertical nitrate fluxes within two CEs. Comparable studies concentrating on Mesoscale eddies are sparse. The turbulent vertical nitrate fluxes presented in this study are among the higher range of those reported by previous studies, especially for an open-ocean setting like CE_2019_18N_20W (see references in Tabel 1 of Cyr et al., 2015). With $1.63 \times 10^{-1} \mu\text{mol m}^{-2} \text{s}^{-1}$ the fluxes in CE_2019_14N_25W are close to $1.18 \times 10^{-1} \mu\text{mol m}^{-2} \text{s}^{-1}$ reported by Schafstall et al. (2010) for the Mauritanian shelf region, where enhanced turbulence was induced by internal tide activity. This supports the idea that CE_2019_14N_25W was strongly influenced by the proximity to topography.

An estimate of the relative importance of the turbulent nitrate fluxes for the highly productive ecosystem of the eddies can be gained by comparing the nitrate fluxes to the total primary production rate (TPP) within the eddies. As it was possible to apply the Redfield (1934) relationship between utilised oxygen and nitrate concentration to the observation area, it is reasonable that the relationship between carbon and nitrogen (6.6 C : N) should also hold. Using this relationship it is possible to compare a nitrate flux to a carbon-based TPP. Quentin Devresse (personal communication) measured TPP during the M160 cruise. On average, the nitrate fluxes of the inner nine stations of CE_2019_18N_20W are capable of explaining 13% of the observed TPP. The observations of TPP in CE_2019_14N_25W revealed a strong non-uniform distribution, which is in general agreement with the widespread distribution of nitrate concentrations and fluxes (Figure 10). The highly elevated nitrate fluxes within CE_2019_14N_25W can sustain 38% of the TPP observed in the eddy. This implies that the high turbulent nitrate fluxes presented in this work are not the main transport mechanism sustaining the primary production. Therefore it is of high importance to undertake further research on the mechanisms, such as advective processes at submesoscale fronts, transporting nutrients into the euphoric zones within eddies.

Given the close proximity to the Cape Verde islands as well as the complex structure, CE_2019_14N_25W can not be considered as an exemplary case for a CE in the ETNA. CE_2019_18N_20W was observed in the open ocean away from interfering topography. Therefore, the dissipation rates and nitrate fluxes observed within this

eddy are more likely to be a representative estimate for CEs within the ETNA. Further research has to be done to consolidate the results presented in this work.

5 References

- Altabet, M.A., Ryabenko, E., Stramma, L., Wallace, D.W.R., Frank, M., Grasse, P., Lavik, G., 2012. An eddy-stimulated hotspot for fixed nitrogen-loss from the Peru oxygen minimum zone. *Biogeosciences* 9 (12), 4897–4908.
- Armi, L., Zenk, W., 1984. Large Lenses of Highly Saline Mediterranean Water. *J. Phys. Oceanogr.* 14 (10), 1560–1576.
- Chaigneau, A., Eldin, G., Dewitte, B., 2009. Eddy activity in the four major upwelling systems from satellite altimetry (1992–2007). *Progress in Oceanography* 83 (1-4), 117–123.
- Chavez, F.P., Messié, M., 2009. A comparison of Eastern Boundary Upwelling Ecosystems. *Progress in Oceanography* 83 (1-4), 80–96.
- Chelton, D.B., Gaube, P., Schlax, M.G., Early, J.J., Samelson, R.M., 2011a. The influence of nonlinear mesoscale eddies on near-surface oceanic chlorophyll. *Science* 334 (6054), 328–332.
- Chelton, D.B., Schlax, M.G., Samelson, R.M., 2011b. Global observations of nonlinear mesoscale eddies. *Progress in Oceanography* 91 (2), 167–216.
- Chelton, D.B., Schlax, M.G., Samelson, R.M., Szoek, R.A. de, 2007. Global observations of large oceanic eddies. *Geophys. Res. Lett.* 34 (15).
- Chouksey, M., Eden, C., Brüggemann, N., 2018. Internal Gravity Wave Emission in Different Dynamical Regimes. *J. Phys. Oceanogr.* 48 (8), 1709–1730.
- Cushman-Roisin, B., Beckers, J.-M., 2011. Introduction to geophysical fluid dynamics: Physical and numerical aspects, 2. ed. ed. Acad. Press, Waltham, Mass, 828 pp.
- Cushman-Roisin, B., Tang, B., Chassignet, E.P., 1990. Westward Motion of Mesoscale Eddies. *J. Phys. Oceanogr.* 20 (5), 758–768.
- Cyr, F., Bourgault, D., Galbraith, P.S., Gosselin, M., 2015. Turbulent nitrate fluxes in the Lower St. Lawrence Estuary, Canada. *J. Geophys. Res.* 120 (3), 2308–2330.
- Ducklow, H., Steinberg, D., Buesseler, K., 2001. Upper Ocean Carbon Export and the Biological Pump. *oceanog* 14 (4), 50–58.
- Efron, B., 1979. Bootstrap Methods: Another Look at the Jackknife. *Ann. Statist.* 7 (1).
- Falkowski, P.G., Ziemann, D., Kolber, Z., Bienfang, P.K., 1991. Role of eddy pumping in enhancing primary production in the ocean. *Nature* 352 (6330), 55–58.

- Fer, I., Bosse, A., Ferron, B., Bouruet-Aubertot, P., 2018. The Dissipation of Kinetic Energy in the Lofoten Basin Eddy. *Journal of Physical Oceanography* 48 (6), 1299–1316.
- Fernández-Castro, B., Evans, D.G., Frajka-Williams, E., Vic, C., Naveira-Garabato, A.C., 2020. Breaking of Internal Waves and Turbulent Dissipation in an Anticyclonic Mode Water Eddy. *J. Phys. Oceanogr.* 50 (7), 1893–1914.
- Fischer, J., Brandt, P., Dengler, M., Müller, M., Symonds, D., 2003. Surveying the Upper Ocean with the Ocean Surveyor: A New Phased Array Doppler Current Profiler. *J. Atmos. Oceanic Technol.* 20 (5), 742–751.
- Gargett, A.E., Osborn, T.R., Nasmyth, P.W., 1984. Local isotropy and the decay of turbulence in a stratified fluid. *Journal of Fluid Mechanics* 144, 231–280.
- Godø, O.R., Samuelsen, A., Macaulay, G.J., Patel, R., Hjøllø, S.S., Horne, J., Kaartvedt, S., Johannessen, J.A., 2012. Mesoscale eddies are oases for higher trophic marine life. *PloS one* 7 (1), e30161.
- Goldthwait, S.A., Steinberg, D.K., 2008. Elevated biomass of mesozooplankton and enhanced fecal pellet flux in cyclonic and mode-water eddies in the Sargasso Sea. *Deep Sea Research Part II: Topical Studies in Oceanography* 55 (10-13), 1360–1377.
- Gregg, M.C., 1999. Uncertainties and Limitations in Measuring ϵ and χ_T . *Journal of Atmospheric and Oceanic Technology* 16 (11), 1483–1490.
- Hales, B., Moum, J.N., Covert, P., Perlin, A., 2005. Irreversible nitrate fluxes due to turbulent mixing in a coastal upwelling system. *J. Geophys. Res.* 110 (C10).
- Hauss, H., Christiansen, S., Schütte, F., Kiko, R., Edvam Lima, M., Rodrigues, E., Karstensen, J., Löscher, C.R., Körtzinger, A., Fiedler, B., 2016. Dead zone or oasis in the open ocean? Zooplankton distribution and migration in low-oxygen modewater eddies. *Biogeosciences* 13 (6), 1977–1989.
- Hood, E., Sabine, C., Sloyan, B., 2010. The GO-SHIP Repeat Hydrography Manual: A Collection of Expert Reports and Guidelines. IOCCP Report Number 14. ICPO Publication Series Number 134. <http://www.go-ship.org/HydroMan.html>.
- Hummels, R., Dengler, M., Rath, W., Foltz, G.R., Schütte, F., Fischer, T., Brandt, P., 2020. Surface cooling caused by rare but intense near-inertial wave induced mixing in the tropical Atlantic. *Nature communications* 11 (1), 3829.

- Ito, T., Follows, M.J., Boyle, E.A., 2004. Is AOU a good measure of respiration in the oceans? *Geophys. Res. Lett.* 31 (17), n/a-n/a.
- Karstensen, J., Fiedler, B., Schütte, F., Brandt, P., Körtzinger, A., Fischer, G., Zantopp, R., Hahn, J., Visbeck, M., Wallace, D., 2015. Open ocean dead zones in the tropical North Atlantic Ocean. *Biogeosciences* 12 (8), 2597–2605.
- Kostianoy, A.G., Belkin, I.M., 1989. A Survey of Observations on Intrathermocline Eddies in the World Ocean. *Elsevier* 50, 821–841. doi:10.1016/S0422-9894(08)70223-X, 821-841.
- Lachkar, Z., Gruber, N., 2012. A comparative study of biological production in eastern boundary upwelling systems using an artificial neural network. *Biogeosciences* 9 (1), 293–308.
- Landschützer, P., Gruber, N., Bakker, D.C.E., Schuster, U., 2014. Recent variability of the global ocean carbon sink. *Global Biogeochem. Cycles* 28 (9), 927–949.
- Lévy, M., Ferrari, R., Franks, P.J.S., Martin, A.P., Rivi re, P., 2012. Bringing physics to life at the submesoscale. *Geophys. Res. Lett.* 39 (14), n/a-n/a.
- L b, J., K hler, J., Mertens, C., Walter, M., Li, Z., Storch, J.-S., Zhao, Z., Rhein, M., 2020. Observations of the Low-Mode Internal Tide and Its Interaction With Mesoscale Flow South of the Azores. *J. Geophys. Res.* 125 (11).
- McGillicuddy, D.J., Anderson, L.A., Bates, N.R., Bibby, T., Buesseler, K.O., Carlson, C.A., Davis, C.S., Ewart, C., Falkowski, P.G., Goldthwait, S.A., Hansell, D.A., Jenkins, W.J., Johnson, R., Kosnyrev, V.K., Ledwell, J.R., Li, Q.P., Siegel, D.A., Steinberg, D.K., 2007. Eddy/wind interactions stimulate extraordinary mid-ocean plankton blooms. *Science* 316 (5827), 1021–1026.
- Menkes, C.E., 2002. A whirling ecosystem in the equatorial Atlantic. *Geophys. Res. Lett.* 29 (11).
- Moum, J.N., Gregg, M.C., Lien, R.C., Carr, M.E., 1995. Comparison of Turbulence Kinetic Energy Dissipation Rate Estimates from Two Ocean Microstructure Profilers. *Journal of Atmospheric and Oceanic Technology* 12 (2), 346–366.
- Nasmyth, P.W., 1970. Oceanic turbulence.
- Oakey, N.S., 1982. Determination of the Rate of Dissipation of Turbulent Energy from Simultaneous Temperature and Velocity Shear Microstructure Measurements. *J. Phys. Oceanogr.* 12 (3), 256–271.

- Olbers, D., Eden, C., 2017. A Closure for Internal Wave–Mean Flow Interaction. Part I: Energy Conversion. *J. Phys. Oceanogr.* 47 (6), 1389–1401.
- Osborn, T.R., 1974. Vertical Profiling of Velocity Microstructure. *J. Phys. Oceanogr.* 4 (1), 109–115.
- Osborn, T.R., 1980. Estimates of the Local Rate of Vertical Diffusion from Dissipation Measurements. *J. Phys. Oceanogr.* 10 (1), 83–89.
- Oschlies, A., Garçon, V., 1998. Eddy-induced enhancement of primary production in a model of the North Atlantic Ocean. *Nature* 394 (6690), 266–269.
- Palacios, D.M., Bograd, S.J., Foley, D.G., Schwing, F.B., 2006. Oceanographic characteristics of biological hot spots in the North Pacific: A remote sensing perspective. *Deep Sea Research Part II: Topical Studies in Oceanography* 53 (3–4), 250–269.
- Prandke, H., Stips, A., 1998. Test measurements with an operational microstructure-turbulence profiler: Detection limit of dissipation rates. *Aquat. Sci.* 60 (3), 191.
- Redfield, A., 1934. On the Proportions of Organic Derivatives in Sea Water and Their Relation to the Composition of Plankton. *James Johnstone Memorial Volume*, 176–192.
- Schafstall, J., Dengler, M., Brandt, P., Bange, H., 2010. Tidal-induced mixing and diapycnal nutrient fluxes in the Mauritanian upwelling region. *J. Geophys. Res.* 115 (C10).
- Schütte, F., Brandt, P., Karstensen, J., 2016a. Occurrence and characteristics of mesoscale eddies in the tropical northeastern Atlantic Ocean. *Ocean Sci.* 12 (3), 663–685.
- Schütte, F., Karstensen, J., Krahmann, G., Hauss, H., Fiedler, B., Brandt, P., Visbeck, M., Körtzinger, A., 2016b. Characterization of “dead-zone” eddies in the eastern tropical North Atlantic. *Biogeosciences* 13 (20), 5865–5881.
- St. Laurent, L., Schmitt, R.W., 1999. The Contribution of Salt Fingers to Vertical Mixing in the North Atlantic Tracer Release Experiment*. *J. Phys. Oceanogr.* 29 (7), 1404–1424.
- Stramma, L., Bange, H.W., Czeschel, R., Lorenzo, A., Frank, M., 2013. On the role of mesoscale eddies for the biological productivity and biogeochemistry in the eastern tropical Pacific Ocean off Peru. *Biogeosciences* 10 (11), 7293–7306.

- Tew Kai, E., Marsac, F., 2010. Influence of mesoscale eddies on spatial structuring of top predators' communities in the Mozambique Channel. *Progress in Oceanography* 86 (1-2), 214–223.
- Weiss, R.F., 1970. The solubility of nitrogen, oxygen and argon in water and seawater. *Deep Sea Research and Oceanographic Abstracts* 17 (4), 721–735.
- Zhang, Z., Zhang, Y., Wang, W., Huang, R.X., 2013. Universal structure of mesoscale eddies in the ocean. *Geophys. Res. Lett.* 40 (14), 3677–3681.

6 Acknowledgements

Here I would like to thank Marcus Dengler for the opportunity to work on this interesting topic and his guidance throughout the work. The fruitful discussions in the Wednesday meetings were well appreciated, for those I would like to thank Tim Fischer, Hannah Melzer, and Johannes Karstensen. Great appreciation goes to Tim Fischer for the post-processing of the microstructure data. I also wish to thank Torge Martin for co-supervising this work.

Finally, I wish to thank my family and friends for constantly supporting me throughout my studies. Without your support and constant interest in my work, this would not have been possible.

Eidesstattliche Erklärung

Hiermit erkläre ich, dass ich die vorliegende Arbeit selbständig und ohne fremde Hilfe angefertigt und keine anderen als die angegebenen Quellen und Hilfsmittel verwendet habe. Die eingereichte schriftliche Fassung der Arbeit entspricht der auf dem elektronischen Speichermedium. Weiterhin versichere ich, dass diese Arbeit noch nicht als Abschlussarbeit an anderer Stelle vorgelegen hat.

Datum: 09.07.2021

Unterschrift: _____

A handwritten signature in black ink, appearing to be 'M. H.' followed by a stylized flourish.